RSC Advances

PAPER

View Article Online
View Journal | View Issue

Cite this: *RSC Adv.*, 2020, **10**, 28343

Tunable broadband-negative-permeability metamaterials by hybridization at THz frequencies

Thi Hien Nguyen, *[a] Son Tung Bui,[b] Xuan Ca Nguyen,[a] Dinh Lam Vu[c] and Xuan Khuyen Bui*[b]

We present a numerical study of thermo-tunable broadband-negative-permeability metamaterial based on second-order hybridization operating at the THz regime. The conventional metal is replaced by InSb, in which the temperature-dependent conductivity plays a key role in tuning the separation of second-order-hybridization magnetic-resonance modes. It is demonstrated that the hybridization in a simple disk-pair dimer can be tuned by temperature, leading to a significant broadening of the negative-permeability at THz frequencies. By increasing the temperature of the InSb patterns in the structure from 300 to 450 K, the fractional bandwidth (FBW) of the negative permeability curve varies from 4.4% to 12.9%. The thermally-increased carrier-density of InSb reduces the kinetic inductance, the main mechanism of the enhanced magnetic-resonance and the stronger activated-hybridization. Moreover, optimization for the bandwidth of negative permeability is also carried out by changing the geometrical parameters to have a FBW of 20.9%. The equivalent LC-circuit model and standard retrieval method are performed to elaborate our proposed idea. Our results would pave the way for the implementations of diversified semiconductors in tunable broadband-negative-permeability and broadband-negative-refractive-index metamaterials at THz frequencies.

Received 25th May 2020
Accepted 17th July 2020

DOI: 10.1039/d0ra04612d

rsc.li/rsc-advances

1. Introduction

In recent years, metamaterials (MMs) have attracted much attention from the scientific community by their unnatural electromagnetic (EM) properties.[1] MMs can be regarded as artificial materials with sub-wavelength unit cell. These unit cells function as atoms in common materials. A "meta-atom" is generally composed of two main components: the electric component allows a negative permittivity ($\varepsilon < 0$) and the magnetic component provides negative permeability ($\mu < 0$). These elements can be arranged either in a periodic or disordered lattice. By carefully designing the electric and magnetic components, one can create exotic properties, for instance, negative refraction,[2,3] perfect absorption,[4–6] invisible cloak[7] and electromagnetically-induced transparency.[8,9] The unusual properties of MMs have been theoretically and experimentally confirmed by numerous studies so far. However, to put the interesting properties of MMs into real applications, in fact, many issues need to be studied and explained in a satisfactory manner. One of the longstanding issues is how to widen the operating frequency band of MMs.[10–15] While a wide negative-permittivity band can be easily achieved using the plasma behavior of a continuous wire medium, a negative-permeability band is often narrow due to the intrinsic resonance of MMs. Therefore, expanding the operating band of negative-permeability MMs has been a key solution for scientists to realize a broadband negative-refractive-index (NRI) behavior. Despite the fact that numerous efforts have been made to overcome this challenge, most of them have been limited in applications for certain reasons, for examples, symmetry breaking, the requirement of rigorous structural adjustments[16,17] or complicated structure shapes.[10,18] With this motivation, we attempted to propose a simple and effective hybridization model to extend the operating frequency band of a negative-permeability and NRI bands.[11–13] The underlying physics of this method is to have additional magnetic resonance, which is split from the original one through a strong plasmonic hybridization. Importantly, the magnetic-resonance split occurs when the energies of the internal and the external couplings are strong and comparable.[11,12] To achieve this, there are two conditions that need to be satisfied. The first condition is the distance between the two monomers (each monomer is composed of two metallic structures that are separated by a dielectric spacer) in a dimer must be well defined.[11–13] This can be overcome by an intensive structural optimization. Meanwhile, the second condition requires that the loss factor should be small or the induced-charge current must be large.[13,19,20] Thus, changing this charge current, based on a hybridization

[a]*Faculty of Physics and Technology, TNU-University of Science, Thai Nguyen, Vietnam. E-mail: hiennt@tnus.edu.vn*

[b]*Institute of Materials Science, Vietnam Academy of Science and Technology, Vietnam. E-mail: khuyenbx@ims.vast.ac.vn*

[c]*Graduate University of Science and Technology, Vietnam Academy of Science and Technology, Vietnam*

scheme, effectively affects the efficiency of separating magnetic-resonance frequencies.

In other words, the dependence of hybridization strength on structural parameters is further verified using the equivalent circuit model.[21] The efficiency of separating magnetic-resonance frequencies in hybridization can be determined by an approximate formula: $\Delta\omega = |\omega_{-+}\rangle - |\omega_{--}\rangle \approx k\omega_0$, where $\Delta\omega$ is the distance between two separated magnetic resonant modes, $k = \frac{M}{L}$ is a coupling coefficient, with L the effective inductance and M the mutual-inductance. Hence, if one can control the value of either L or M, the efficiency of separating asymmetric magnetic-resonance frequencies is tunable. For this purpose, one can integrate a semiconductor into conventional MMs. According to the Drude model, the carrier density in a semiconductor depends solely on temperature. Consequently, by doping semiconductors into the MM structure, the value of conductivity of the metallic component can be thermally manipulated. Consequently, the value of the effective inductance can be thermally controlled. By incorporating the MMs with an appropriate temperature controller, for instance, a continuous flow liquid helium cryostat, their thermo-dependent properties can be realized almost instantaneously.[22,23]

Recently, we have shown that a tunable meta-magnetic resonator (in a disk-pair structure) can be realized by using InSb as a mutable metal.[24] Hence, in this work, to achieve a tunable broadband negative permeability (where the asymmetric resonant split in plasmonic hybridization operates effectively), we doped InSb in a symmetric and simple disk-pair dimer (DPD) for the two-layer case. It is demonstrated that the hybridization effect in basic DPD structures is tuned by temperature, resulting in a significant broader THz resonant region.

2. Analytical model and computational setup

A computational unit cell of the InSb DPD is shown in Fig. 1(a), which consists of two monomers separated by the TPX™ polymethylpentene (PMP) film with thickness $d = 10$ μm, dielectric constant of 2.1 and loss tangent of 0.0008. In order to have a strong hybridization effect, PMP is chosen because of its stability in high-temperature and optically transparency in THz ranges and low dielectric constant like that of air.[25,26] The monomers based on the symmetrical DPD structure are made of an InSb semiconductor with thickness t_m and arranged on the top and bottom of a dielectric spacer with thickness t_d. Pyrex glass with a dielectric constant of 4.82 and a loss tangent of 0.0054 is chosen as the dielectric material because of its stability in high-temperature applications.[27,28] The arrangement of the two disk-pair layers and the dielectric layers are consistent with lithography fabrication techniques in the THz region, including evaporation and patterning processes.[29] In our investigations, the DPD is embedded in a reference medium, chosen as a vacuum, and the EM properties of the DPD are simulated by using a commercial CST Microwave Studio.[30] The propagation direction of the incident EM wave is perpendicular to the sample plane, as shown in Fig. 1. The effective permittivity, permeability and refraction index (ε, μ, n) were calculated from simulated transmission and reflection by using the standard retrieval method proposed by Chen.[31]

Fig. 1(a) shows the DPD structure, which is a modification from the well-known cut-wire-pair (CWP) dimer.[11,12] The improvement of the proposed structure is a highly symmetric geometry that makes the MM polarization-insensitive.[19] Similar to EM behaviors in the CWP, the total electromagnetic response of a single disk-pair can be regarded as a hybridization effect between the surface plasmons of two individual disks. This coupling results in two new plasmonic modes: the symmetric $|\omega_+\rangle$ and the anti-symmetric mode $|\omega_-\rangle$, corresponding to in-phase and out-of-phase charge oscillations in the two disks, respectively. The symmetric mode effectively operates as two electric dipoles, while the anti-symmetric mode behaves as a magnetic resonance. In this paper, in order to obtain the broadband negative permeability, we only focus on the anti-symmetric mode with the magnetic resonance behavior. Similar to the CWP dimer,[11,12] the EM response of a DPD can analogously be described by second-order hybridization, as shown in Fig. 1(c). If two disk-pairs are close to each other, the interaction between the degenerated anti-symmetric modes leads to the $|\omega_{--}\rangle$ and $|\omega_{-+}\rangle$ modes. Since both the $|\omega_{--}\rangle$ and $|\omega_{-+}\rangle$ modes are magnetic resonances, stronger second-order hybridization also broadens the bandwidth of the negative permeability. As shown in previous work, tuning the distance (d) between two layers or spacer thickness (t_d) allows us to manipulate the effectiveness of the second-order hybridization.[11,12] Besides, the dependence of the hybridization strength on d and t_d was further verified using the equivalent circuit model.[21] The magnetic plasmon eigen-frequencies are approximately calculated by:

$$|\omega_{--/-+}\rangle = \frac{\omega_0}{\sqrt{1 \pm k}} \quad (1)$$

where $k = \frac{M}{L}$, is a coupling coefficient,[11,19] and ω_0 is the resonance frequency of the individual disk-pair monomer. The mutual-inductance M between two disk-pair monomers in the k-direction is approximately calculated by:[32]

$$M = \frac{\mu_0 (S)^2}{4\pi r^3}\left(1 + jk_0 r - {k_0}^2 r^2\right)\mathrm{e}^{-jk_0 r} \quad (2)$$

Here, k_0 is the wave number at the resonant frequency of the disk-pair monomer, $r = 3 \times t_d + d$ is the distance between the two magnetic dipoles[11,32] and S is the magnetic flux area.

It can be noted that, in the THz region, the total inductance L of the disk-pair is determined by:

$$L = (L_m + L_{mk}) \quad (3)$$

where L_m (disk-inductance) and L_{mk} (the kinetic inductance for the disk) are expressed as:[22,33]

$$L_m = \frac{\pi\mu(t_d + 2t_m)}{4} \text{ and } L_{mk} = \frac{\pi m^*}{2t_m N e^2} \quad (4)$$

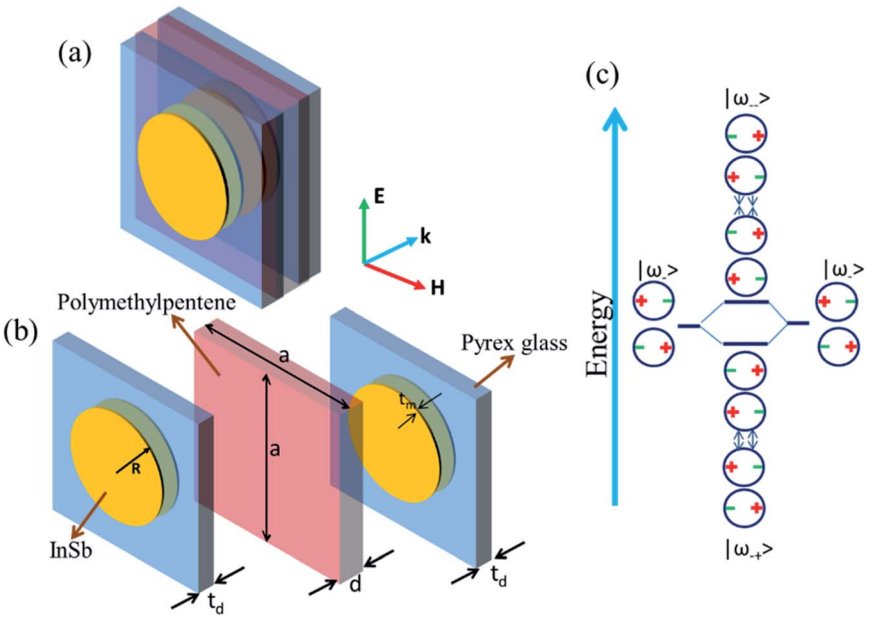

Fig. 1 (a) A unit cell of the disk-pair dimer (DPD) with the polarization of an EM wave. (b) Constituent components of the disk-pair dimer with its geometrical parameters: $a = 62$ μm, $R = 25$ μm, $t_d = 10$ μm, $t_m = 2$ μm and $d = 10$ μm. (c) Corresponding hybridization scheme of the DPD structure.

μ, N, e and m*are the permeability of the Pyrex glass, the carrier density, the electronic charge and the effective mass of free carriers, respectively. Due to $k \ll 1$, therefore, the distance between two separated magnetic resonant modes is calculated by the approximate formula:

$$\Delta\omega = |\omega_{-+}\rangle - |\omega_{--}\rangle \approx k\omega_0 \tag{5}$$

$$\Delta\omega \approx \frac{M}{L}\omega_0 = \frac{\mu_0(S)^2\left(1 + jk_0r - {k_0}^2r^2\right)e^{-jk_0r}}{(4\pi r^3)\left(\frac{\pi\mu(t_d + 2t_m)}{4} + \frac{\pi m^*}{2t_m Ne^2}\right)}\omega_0 \tag{6}$$

In the far infrared region, in principle, the intrinsic carrier concentration between 200 and 798 K of InSb is very well described by the following empirical formula:

$$N = 2.9 \times 10^{11}(2400 - T)^{0.75}\left(1 + 2.7 \times 10^{-4}\ \mathrm{T}\right)T^{1.5}$$

$$\times\exp\left(-\frac{0.129 - 1.5 \times 10^{-4}\ \mathrm{T}}{kT}\right) \tag{7}$$

where T is the absolute temperature and k_B is the Boltzmann constant.[34] From eqn (6) and (7), increasing the temperature results in a raise of charge carrier density N, which eventually reduces the value of kinetic inductance. In other words, the increase of $\Delta\omega$ allows us to effectively enhance the second-order hybridization.

At the same frequency range, the permittivity of InSb can be determined according to the Drude model:[20,35]

$$\varepsilon = \varepsilon_\infty - \frac{{\omega_p}^2}{\omega^2 + i\gamma\omega} \tag{8}$$

where ε_∞, ω, γ, ω_p are the high-frequency permittivity limit, the angular frequency, the damping constant and the plasma frequency, respectively. The plasma frequency is defined as:

$$\omega_p = \left(\frac{Ne^2}{\varepsilon_0 m^*}\right)^{\frac{1}{2}} \tag{9}$$

in which ε_0 is the vacuum permittivity. In fact, the damping constant (γ) of InSb is strongly dependent on the electron mobility.[22,24] However, in the temperature range of interest (from 300 to 450 K), within a frequency region from 0.1 to 1.7 THz, the electron mobility depends solely on the applied temperature.[36,37] For this reason, the influence of temperature on the damping constant can be neglected. The values of the parameters of InSb are $\varepsilon_\infty = 15.68$, $\gamma = 5 \times 10^{10}$ Hz and $m^* = 1.37 \times 10^{-32}$ kg.[20,35] After an optimization process, a periodicity (a) of 62 μm is chosen to avoid unwanted interaction between adjacent disk-pairs on the same plane.[22,24] The thicknesses of the Pyrex glass dielectric spacer (t_d), the InSb semiconductor (t_m) and the radius of the disk (R) are optimized to be 10, 2, and 25 μm, respectively.

3. Results and discussions

From eqn (7) and (9), we can calculate the dependences of carrier density and plasma frequency on temperature, as shown in Fig. 2. It can be observed that an increase of temperature gives rise to an increased carrier density and plasma frequency. Consequently, InSb has a more-metallic feature, which plays an important role for separating hybridized-magnetic-resonance frequencies by temperature.

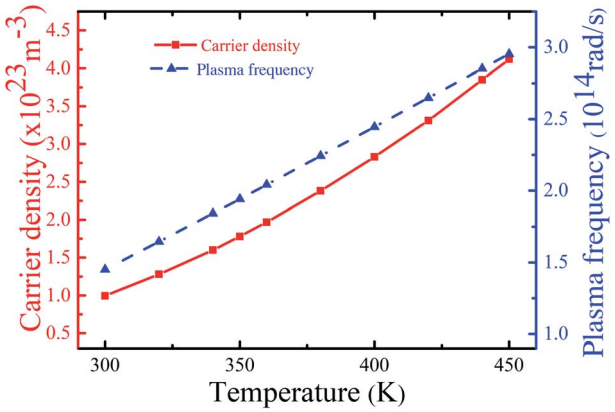

Fig. 2 Calculated carrier density (red solid line) and plasma frequency (blue dashed line) of InSb according to the applied temperature.

Substituting these calculated results (in Fig. 2) into the Drude model for InSb in CST, transmission coefficients at different temperatures were simulated, as shown in Fig. 3(a). The DPD structure exhibits transmission dips in the spectra when an external field is applied. This phenomenon is well known as the magnetic resonance induced by the coupling of the DP monomer to the **H** field, leading to the narrow stop-band. For the DP dimer, similar to the CWP dimer in ref. 11 and 12, this stop-band can be expanded when the hybridization is activated. Fig. 3(a) shows that there is only one narrow stop-band at a low temperature (T = 300 K). By increasing the temperature, the stop band gradually becomes wider and finally splits into two stop-bands (around 1.27 and 1.3 THz) at $T = 450$ K. In order to verify the existence of a negative permeability, the standard retrieval method proposed by Chen is performed by applying transmission, refraction and phase parameters. The retrieved values of effective permeability dependent on temperature are presented in Fig. 3(b). It is clearly seen that a region of negative permeability is achieved and wider when the temperature is increased from 300 to 450 K. The ratio of the bandwidth for negative permeability to operating frequency $\left(= \frac{2(f_{\max(\mu<0)} - f_{\min(\mu<0)})}{f_{\max(\mu<0)} + f_{\min(\mu<0)}}\right)$ increased from 4.4% to 12.9% as the temperature changed from 300 to 450 K. The obtained negative permeability is also evidence of the existence of magnetic resonance. Importantly, the negative-permeability band becomes gradually wider and splits into two peaks when the temperature is increased. The expansion of the magnetic-resonance region can be explained by the LC circuit model. Increasing the temperature results in a raise of the charge carrier density N and eventually reduces the value of the kinetic inductance [follow eqn (5)], and therefore $\Delta\omega = |\omega_{-+}\rangle - |\omega_{--}\rangle \approx k\omega_0$ is increased. Consequently, the stop-band is expanded and separated into two new resonance regions, as presented in Fig. 3(a) and (b).

Besides, the results show that there is a shift of magnetic resonance region from 1.01 THz to 1.3 THz when InSb is heated (from 300 to 450 K). The blue-shift of magnetic resonance can be explained by using the equivalent LC model, as reported in our previous work,[22,24] in which the carrier density is increased by increasing the applied temperature. However, an enhancement of carrier density reduces the value of kinetic inductance and increase the original magnetic resonance frequency $|\omega_{-}\rangle$.[22,24] The shift of the original magnetic resonance mode $|\omega_{-}\rangle$, leads to the shift of the split-magnetic-resonance modes ($|\omega_{--}\rangle$ and $|\omega_{-+}\rangle$) caused by the second-order hybridization effect.

To get more insight into the magnetic resonance mechanism, the distributions of the induced magnetic- and electric-energies (coordinated plane is selected as (**E**, **H**) along the k-vector direction) for different temperatures, 300 K (at 1.01 THz), 350 K (at 1.15 THz), 400 K (at two split peaks of 1.22 THz and 1.25 THz) and 450 K (at two split peaks of 1.27 THz and 1.3 THz), are simulated, as shown in Fig. 4 and 5. It can be seen that the magnetic energy is concentrated around the center area of the disks, whereas the electric energy is mainly located at the ends of them (along the **E** direction), for separated peaks in the temperature range from 300 to 450 K. This observation confirms that the nature of these resonances is magnetic resonance. Owing to the strong coupling between the MM and the

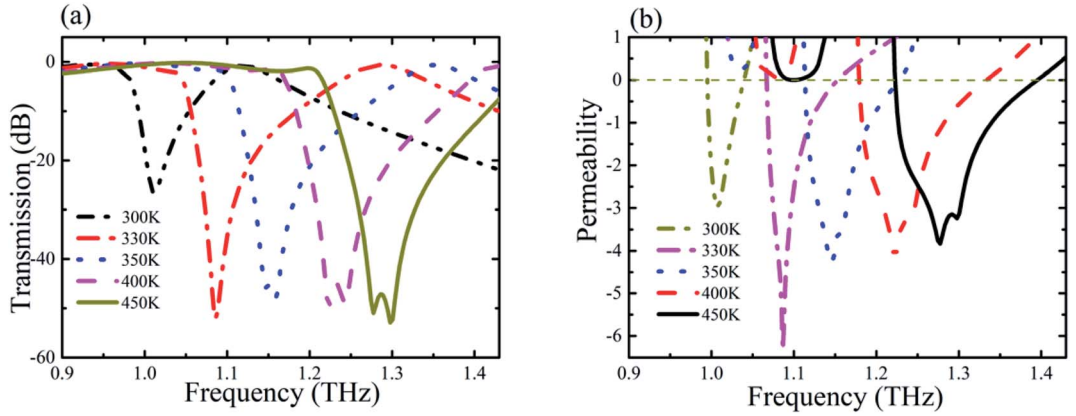

Fig. 3 Dependence of the simulated (a) transmission of DPD and (b) real part of the effective permeability on applied temperature.

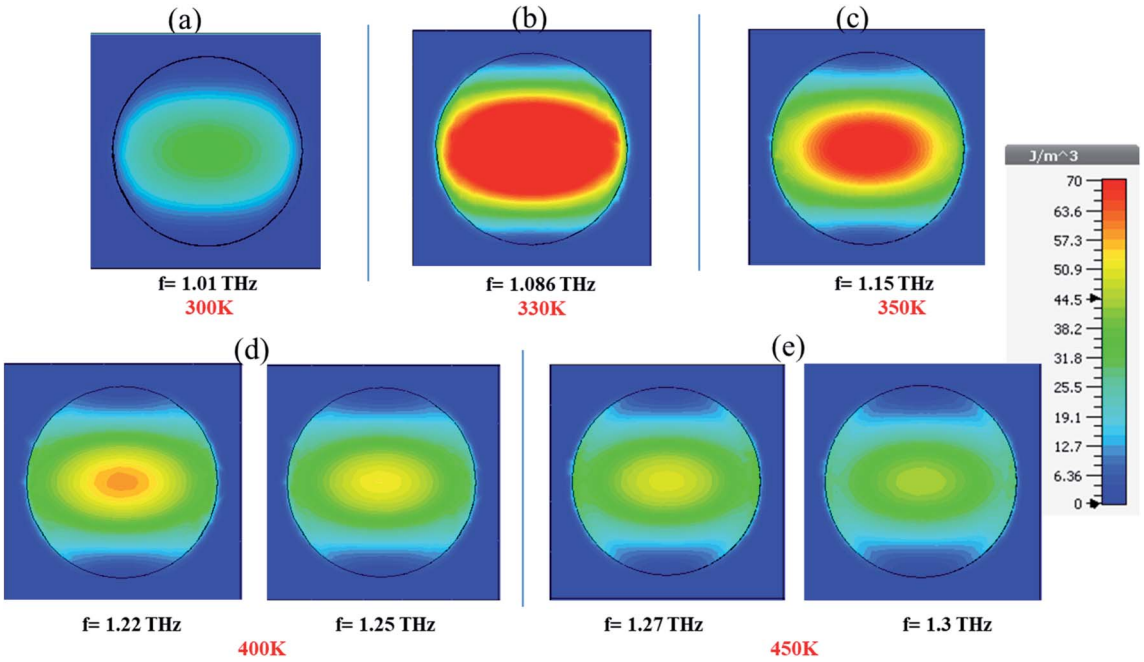

Fig. 4 Magnetic-energy distributions according to temperatures of (a) 300 K at $f = 1.01$ THz, (b) 330 K at $f = 1.086$ THz, (c) 350 K at $f = 1.15$ THz, (d) 400 K at $f = 1.22$ and 1.25 THz and (e) 450 K at $f = 1.27$ and 1.3 THz.

magnetic component of the EM wave, anti-parallel currents are generated on paired disks along the **E** direction. Therefore, charges are accumulated at the ends of each disk that leads to a strong located electric energy in this region.[24] These results also indicate the magnetic origin of the extension resonance regions based on the second-order hybridization scheme.

By exploiting eqn (1)–(7), the distance between two separated magnetic-resonance modes ($\Delta\omega = |\omega_{-+}\rangle - |\omega_{--}\rangle$) of the disk-

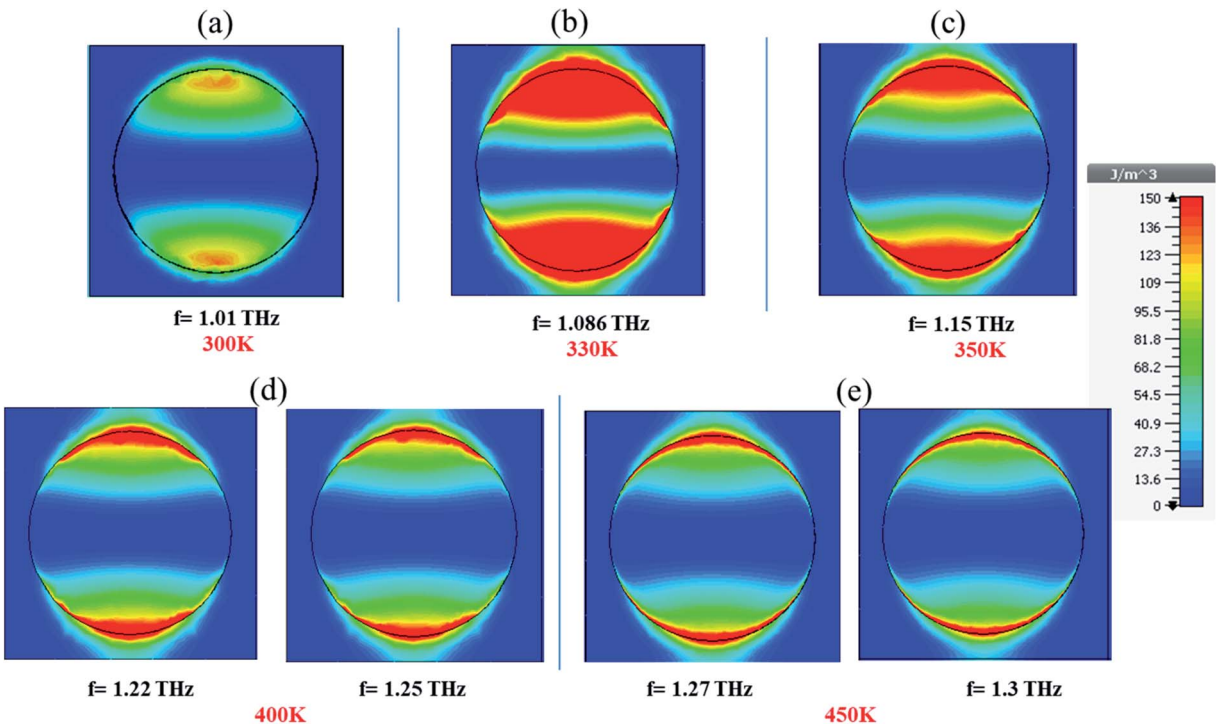

Fig. 5 Electric-energy distributions according to temperatures of (a) 300 K at $f = 1.01$ THz, (b) 330 K at $f = 1.086$ THz, (c) 350 K at $f = 1.15$ THz, (d) 400 K at $f = 1.22$ and 1.25 THz and (e) 450 K at $f = 1.27$ and 1.3 THz.

Table 1 Calculated and simulated separations between two hybridized magnetic-resonance frequencies of disk-pair structure as functions of T

	$T = 300$ K	$T = 350$ K	$T = 400$ K	$T = 450$ K
Calculated separation	1.13×10^{-3} THz	4.71×10^{-3} THz	1.413×10^{-2} THz	2.986×10^{-2} THz
Simulated separation	≈ 0	1.351×10^{-2} THz	1.965×10^{-2} THz	2.67×10^{-2} THz

pair structure can be calculated as functions of T and simultaneously compared with simulated CST results (see Table 1). Based on the distribution of the induced magnetic-energy in Fig. 4, the shape of the magnetic flux areas is nearly close to a rectangle, so the magnetic-flux area in eqn (3) is approximately estimated by $S \approx c_1 R t_d$ (with $c_1 < 1$).

In Table 1, the simulation results were determined from dips in the negative-permeability curves according to the retrieval method proposed by Chen *et al.*[31] It should be noted that both calculated and simulated results show the same tendency for the separation between magnetic resonances. At $T = 300$ K, owing to the large kinetic inductance, the coupling coefficient of hybridization is small, leading to a near non-separation. However, $|\omega_-\rangle$ gradually splits when T increases from 300 to 450 K. $T = 400$ K and $= 450$ K results in a complete resonance-split owing to the higher coupling coefficient, which shows a good coincidence with the hybridization model.

For the hybridization effect, besides, the thickness of the spacer (t_d) determines the internal coupling between two meta-atoms in a monomer while the distance d is responsible for the external-coupling strength among two monomers.[11–13] Hence, the relation between d and t_d plays a key role in the effectiveness of the second-order hybridization. To maximize the bandwidth of negative permeability and simultaneously prove the expanded negative permeability is the result of magnetic resonance frequency separation according to the second-order hybridization scheme, we adjusted the structural parameters d and t_d with temperature fixed at 450 K. Fig. 6(a) and (b)

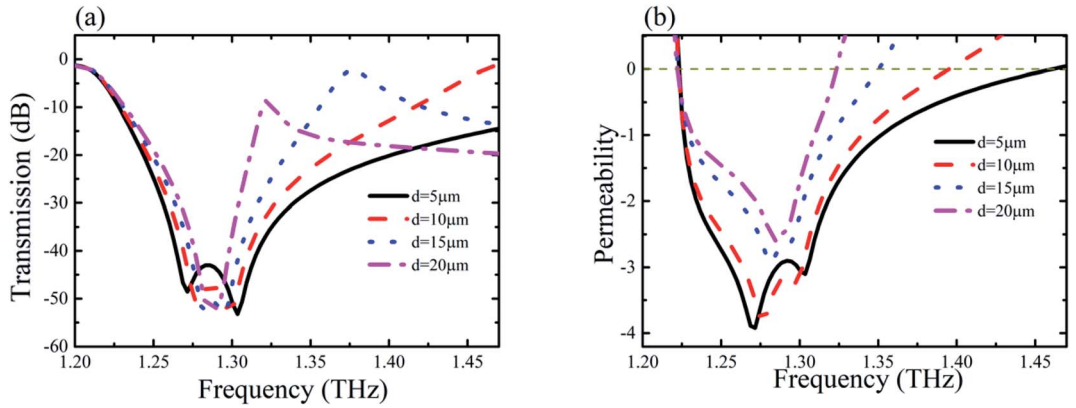

Fig. 6 (a) Simulated transmission according to d. (b) Dependence of calculated permeability on d (t_d is kept at 10 μm). All other geometrical parameters are unchanged.

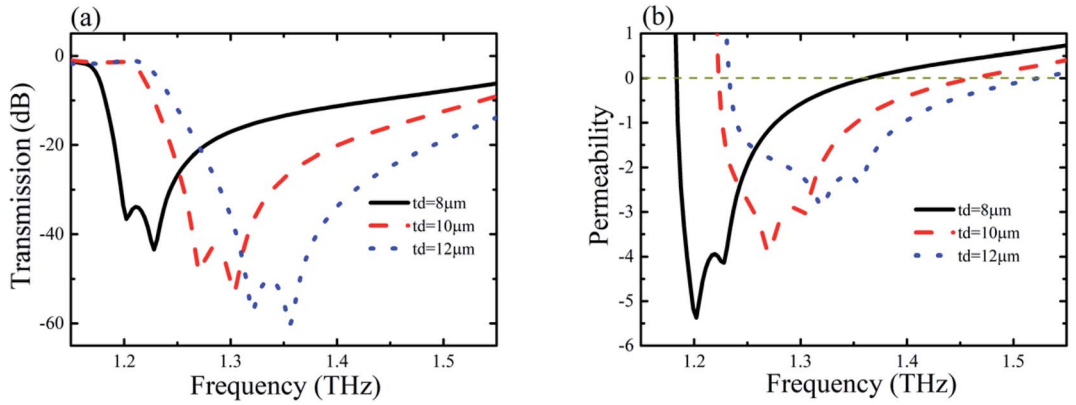

Fig. 7 (a) Simulated transmission according to t_d. (b) Dependence of calculated permeability on t_d (d is kept at 5 μm). All other geometrical parameters are unchanged.

present the simulated transmission spectra and calculated permeability according to d with t_d fixed at 10 μm at 450 K. It is shown that when the external coupling is strengthened by decreasing d, the resonance band is wider. In this case, the ratio of the bandwidth negative permeability to the operating frequency enhances from 12.3% to 17.5%, when d reduces from 20 to 5 μm. Then, the optimization is continued by changing the distance t_d with d fixed at 5 μm. Fig. 7(a) and (b) show the simulated transmission spectra and calculated permeability values of the DPD as a function of t_d. Obviously, the resonance band with negative permeability is also significantly wider (from 13.9% to 20.9%) when t_d is changed from 8 to 12 μm.

The results in Fig. 6 and 7 manifest that the EM response of the DPD can be expressed *via* the interplay between the internal and the external couplings. The broadband negative-permeability region is activated effectively when these two interactions are energetically comparable to each other. These results are entirely consistent with the split of the original magnetic resonance in the second-order hybridization in ref. 11–13.

The broadband negative permeability was also achieved in the results of previous work. In the GHz band, negative permeability bandwidths of 28% (from 15 to 20 GHz) by using S-shape resonators,[38] 60% by using a periodic cage of backward-wave transmission lines[39] and 45.3% by using four-cell slabs[40] were recorded. In the THz band, a broadband negative permeability was also achieved up to 50% by adjusting the Mie resonance through the structural parameters of a single type of rod.[41] However, to achieve a broadband negative permeability almost all previous work used the method of optimizing parameters of the structure and geometry or using contra-directional coupling between a backward wave guided by a transmission line and a forward, free-space wave. In another way, our results indicate that a broadband negative permeability is achieved by thermally-tunable hybridization. Our results pave the way for the implementations of diversified semiconductors in tunable broadband negative permeability metamaterials at THz frequencies.

4. Conclusions

A thermo-tunable broadband-negative-permeability based on second-order hybridization in MM operating at THz frequencies was demonstrated numerically. The active tunability of the broadband-negative-permeability was carried out by thermal control to enhance the carrier density of InSb in a DPD structure. The investigation showed that not only is the separation efficiency of hybridization magnetic-resonances effectively controlled but also the negative-permeability band is significantly expanded when the temperature is increased. Our results pave the way for implementations of negative-permeability MMs in the next generation of active MM-devices at THz frequencies.

Conflicts of interest

There are no conflicts to declare.

Acknowledgements

This research was funded by the Vietnam National Foundation for Science and Technology Development (NAFOSTED) under Grant No. "103.99-2018.35". This work was supported by the Institute of Materials Science, Vietnam Academy of Science and Technology under Grant No. CS.05/20-21.

References

1 V. G. Veselago, The electrodynamics of substances with negative ε and μ, *Sov. Phys. Usp.*, 1968, **10**, 509–514.
2 T. T. Shuaishuai, R. Chunyu and T. Weipeng, High-transmission negative refraction in the gradient space-coiling metamaterials, *Appl. Phys. Lett.*, 2019, **114**, 204101.
3 N. P. Gandji, G. B. Semouchkin and E. Semouchkina, All-dielectric metamaterials: irrelevance of negative refraction to overlapped Mie resonances, *J. Phys. D: Appl. Phys.*, 2017, **50**, 455104.
4 P. Kevin, K. Matthias, B. Julian, B. Andre, A. Philipp, K. Ulrich and R. Stefan, Random anti-lasing through coherent perfect absorption in a disordered medium, *Nature*, 2019, **567**, 351.
5 T. V. Huynh, B. S. Tung, B. X. Khuyen, N. S. Tung, V. D. Lam and N. T. Tung, *Comput. Mater. Sci.*, 2019, **166**, 276.
6 B. X. Khuyen, B. S. Tung, N. T. Tung, N. T. Hien, Y. J. Kim, L. Y. Chen, Y. P. Lee, P. T. Linh and V. D. Lam, Realization for dual-band high-order perfect absorption, based on metamaterial, *J. Phys. D: Appl. Phys.*, 2020, **53**, 105502.
7 J. B. Pendry, D. Schurig and D. R. Smith, Controlling electromagnetic fields, *Science*, 2006, **312**, 1780.
8 J. S. Hwang, B. S. Tung and Y. P. Lee, Electromagnetically-induced Transparency in Metamaterials for the Potential Applications, *J. Korean Phys. Soc.*, 2018, **72**, 1491.
9 R. Kun, H. Yumeng, R. Xiaobin, Z. Ying, H. Qun, W. Liedong and X. Maojun, Dynamically tunable multi-channel and polarization-independent electromagnetically induced transparency in terahertz metasurfaces, *J. Phys. D: Appl. Phys.*, 2020, **53**, 122593.
10 S. Zhou, S. Townsend, Y. M. Xie, X. Huang, J. Shen and Q. Li, Design of fishnet metamaterials with broadband negative refractive index in the visible spectrum, *Opt. Lett.*, 2014, **39**, 2415.
11 N. T. Tung, D. T. Viet, B. S. Tung, N. V Hieu, P. Lievens and V. D. Lam, Broadband Negative Permeability by Hybridized Cut-Wire Pair Metamaterials, *Appl. Phys. Express*, 2012, **5**, 112001.
12 N. T. Tung, B. S. Tung, E. Janssens, P. Lievens and V. D. Lam, Broadband negative permeability using hybridized metamaterials: Characterization, multiple hybridization, and terahertz response, *J. Appl. Phys.*, 2014, **116**, 083104.
13 N. T. Hien, B. S. Tung, Y. Sen, A. E. V. Guy, P. Lievens, V. D. Lam and J. Ewald, Broadband negative refractive index obtained by plasmonic hybridization in metamaterials, *Appl. Phys. Lett.*, 2016, **109**, 221902.
14 L. Fang, Z. Zheqiang, Z. Yuan, H. Renshuai and Z. Bin, Broadband negative-refractive index terahertz metamaterial

with optically tunable equivalent-energy level, *Opt. Express*, 2018, **26**, 30085.
15 L. Fang, Z. Zheqiang, H. Renshuai and Z. Bin, A broadband tunable terahertz negative refractive index metamaterial, *Sci. Rep.*, 2018, **8**, 9843.
16 Z. Wei, Y. Cao Y, J. Han, C. Wu, Y. Fan and H. Li, Broadband negative refraction in stacked fishnet metamaterial, *Appl. Phys. Lett.*, 2010, **97**, 141901.
17 A. C. Atre, A. Garcıa-Etxarri, H. Alaeian and J. A. Dionne, A broadband negative index metamaterial at optical frequencies, *Adv. Opt. Mater.*, 2013, **1**, 327.
18 J. Gielis, A generic geometric transformation that unifies a wide range of natural and abstract shapes, *Am. J. Bot.*, 2003, **90**, 333.
19 N. T. Hien, L. D. Hai, B. S. Tung, B. X. Khuyen, N. X. Ca and V. D. Lam, Plasmonic hybridization in symmetric metamaterial for broadband negative refractive index: simulation, experiment and characterization, *J. Phys. D: Appl. Phys.*, 2020, **53**, 175501.
20 Q. Bai, C. Liu, J. Chen, C. Cheng, M. Kang and H. T. Wang, Tunable slow light in semiconductor metamaterial in a broad terahertz regime, *J. Appl. Phys.*, 2010, **107**, 093104.
21 L. Zhu, F. Meng, J. Fu, Q. Wu and J. Hua, Multi-band slow light metamaterial, *Opt. Express*, 2012, **20**, 4494.
22 N. T. Hien, L. N. Le, P. T. Trang, B. S. Tung, N. D. Viet, P. T. Duyen, N. M. Thang, D. T. Viet, Y. P. Lee, V. D. Lam and N. T. Tung, Characterizations of a thermo-tunable broadband fishnet metamaterial at THz frequencies, *Comput. Mater. Sci.*, 2015, **103**, 189.
23 R. Singh, A. K. Azad, Q. X. Jia, A. J. Taylor and H. T. Chen, Thermal tunability in terahertz metamaterials fabricated on strontium titanate single-crystal substrates, *Opt. Lett.*, 2011, **36**, 1230.
24 B. S. Tung, N. V. Dung, B. X. Khuyen, N. T. Tung, P. Lievens, Y. P. Lee and V. D. Lam, Thermally tunable magnetic metamaterials at THz frequencies, *J. Opt.*, 2013, **15**, 075101.
25 https://www.janis.com/Products/AccessoriesandAncillaryEquipment/WindowTransmissionCurves.aspx.
26 https://www.mitsuichemicals.com/tpx_cha.htm.
27 W. Espe, *Materials of High Vacuum Technology*, Pergamon Press, London, 1968.
28 www.iwakiglassindonesia.com.
29 H. Tao, N. I. Landy, C. M. Bingham, X. Zhang, R. D. Averitt and W. J. Padilla, A metamaterial absorber or the terahertz regime: design, fabrication and characterization, *Opt. Express*, 2008, **16**, 7181.
30 https://www.3ds.com/products-services/simulia/products/cst-studio-suite/?utm_source=cst.com%26utm_medium=301%26utm_campaign=cstfor%20ComputerSimulation%20Technology%20Studio%20Suite.
31 X. Chen, T. M. Grzegorczyk, B. I. Wu, J. Pacheco and J. A. Kong, Robust method to retrieve the constitutive effective parameters of metamaterials, *Phys. Rev. E: Stat., Nonlinear, Soft Matter Phys.*, 2004, **70**, 016608.
32 L. Solymar and E. Shamonina, *Waves in metamaterials*, Oxford University, 2009.
33 S. S. Mohan, Ph.D. Thesis, Stanford University, 1999, pp. 153–155.
34 M. Oszwaldowski and M. Zimpel M, Temperature dependence of intrinsic carrier concentration and density of states effective mass of heavy holes in InSb, *J. Phys. Chem. Solids*, 1988, **49**, 1179.
35 J. Han and A. Lakhtakia, Semiconductor split-ring resonators for thermally tunable terahertz metamaterials, *J. Mod. Opt.*, 2009, **56**, 554.
36 D. L. Rode, Electron transport in InSb, *Phys. Rev. B: Solid State*, 1971, **3**, 3287.
37 J. Zhu, J. Han, Z. Tian, J. Gu, Z. Chen and W. Zhang, Thermal broadband tunable terahertz metamaterials, *Opt. Commun.*, 2011, **284**, 3129.
38 H. Chen, X. Zhang and J. Huangfu, Left-handed material composed of only S-shaped resonators, *Phys. Rev. E: Stat., Nonlinear, Soft Matter Phys.*, 2004, **70**, 057605.
39 M. R. Scott and A. Grbic, Volumetric negative-refractive-index medium exhibiting broadband negative permeability, *J. Appl. Phys.*, 2007, **102**, 013904.
40 M. R. Scott, P. Carl and A. Grbic, Design and Free-Space Measurements of Broadband, Low-Loss Negative-Psermeability and Negative-Index Media, *IEEE Trans. Antennas Propag.*, 2011, **59**, 2989–2997.
41 R. Yahiaoui, H. Němec, P. Kužel, F. Kadlec, C. Kadlec and P. Mounaix, Broadband dielectric terahertz metamaterials with negative permeability, *Opt. Lett.*, 2009, **34**, 3541–3543.

